



Investigations on the influence of manufacturing and curing effects on the properties of structural-glazing adhesives subjected to tensile stresses

Paul Müller · Christian Schuler · Geralt Siebert

Received: 20 January 2023 / Accepted: 30 May 2023
© The Author(s) 2023

Abstract Demand for structural glazing joints has increased considerably in recent years due to the ever-increasing loads resulting from growing dimensions, especially in spectacular glass structures. Within the scope of planning and production monitoring, existing influences are analyzed based on the standard H-sample from the current structural glazing guidelines. These guidelines do not define any specific methodology or guidance for manufacturing test specimens. For determining load-bearing properties, various parameters, such as specimen age and curing condition, have a relevant influence during and after manufacturing. This study aims to investigate the manufacturing process for H-specimens systematically to identify and minimize the interfering influences. On this basis, the influence of the curing of modified H-specimens was investigated in detail for specimens under tensile load. Next to curing at room temperature, tempering at 40 °C was investigated for two different H-joint geometries. Thereby, a relevant influence of specimen age and different curing conditions on the strength as well as stiffness properties could be determined. As one result of the study, the

curing time can be shortened by tempering the specimens in relation to the specified 28 days by ETAG 002-1. For calculation methods used in practice, like the structural spring method, suggestions for statistically validated strength and stiffness parameters representing the load-bearing behavior are proposed, considering the adhesive's curing state and the joint's nominal stress.

Keywords Structural glazing · Civil engineering · Silicones · Curing · Manufacturing · Joint properties

1 Introduction

Structural glazing (SG) has become widely accepted for connecting glass elements as an alternative to mechanical mountings when using glass in construction. The used silicone elastomers can be assigned to the class of rubber-like materials (Treloar 1975), which results in a complex mechanical behavior (Martins et al. 2006; Meunier et al. 2008). This behavior depends on numerous factors. Several of these properties have been addressed in scientific research. The general load-bearing behavior and first suggestions for the design of structural silicone bonds are given in (Hagl 2006, 2007). In (White et al. 2012; van Lancker et al. 2016; Wallau et al. 2021), the influence of environmental factors, like temperature, humidity, ultraviolet radiation, and cyclic movement, on the durability of sealant systems was investigated. (Schuler et al. 2017; Bues

P. Müller (✉) · C. Schuler
Institute for Material and Building Research, Munich
University of Applied Science HM, Karlstraße 6, 80333
Munich, Germany
e-mail: mueller.paul@hm.edu

G. Siebert
Faculty of Civil Engineering and Environmental Science, University of the Bundeswehr Munich, Werner-Heisenberg-Weg 39, 85579 Neubiberg, Germany

et al. 2019; Bues 2021) researched the load-bearing behavior of joint-like samples under geometry, temperature, and moisture aging modifications and proposed a tension-shear interaction and a cavitation-based failure criterium.

In Schuler et al. (2017), initial results were obtained on the influence of artificial heat aging on SG silicones. Based on shear-stressed single-lap joint specimens, no influence of temperature aging on strength or stiffness could be determined. Based on shear-stressed H-specimens, strength and stiffness were increased due to heat aging at 45 °C for 21 and 42 days, compared with the reference specimen. No relevant influence was observed due to the different aging times. The reference specimens were cured at RT for 7 days and afterward annealed at 45 °C for 6 h.

The numeric representation of the deformation behavior by extended hyperelastic material models was part of several investigations (Dias et al. 2014; Richter 2018; Drass 2020; Rosendahl 2020; van Lancker et al. 2020). In addition, efforts have been devoted to defining criteria for predicting failure (Santarsiero 2015; Descamps et al. 2017; Staudt et al. 2018; Richter et al. 2021). All these approaches have in common that developing and calibrating a complex and time-consuming numerical model is necessary.

A method for determining a semi-probabilistic material safety factor for SG-silicones is proposed in (Drass and Kraus 2020b; Kraus and Drass 2020), where the material properties of joints exposed to different temperature conditions and after artificial aging are investigated. A Eurocode-compliant approach to using FEM is suggested by (Drass and Kraus 2020a).

From a normative point of view, for designing SG joints in curtain wall facades, (ETAG 002-1, ASTM C1401-14, DIN EN 13022-1:2014-08, EN 13830:2015 + A1:2020) define concepts for quality assurance and simplified calculation methods. The width h_c and thickness e of SG joints of four-sided fixed glass panes can be calculated via (1) and (2) from (ETAG 002-1). These expressions can only be applied when the joint geometry complies with the boundaries in (3–5). For joint geometries beyond the scope of the (ETAG 002-1), further investigations are needed to account for the volumetric load-bearing behavior of the SG silicones.

To ensure an economical and safe planning process, comparatively high global safety factors cover the existing uncertainties and inaccuracies. σ_{des} is calculated via (6) to account for these uncertainties and

inaccuracies, which arise on the material side due to environmental or manufacturing influences and on the design side due to simplified material models and analytical approaches as described in the previous paragraphs.

$$h_c \geq \left| \frac{aw}{2\sigma_{des}} \right| [\text{mm}] \quad (1)$$

$$e \geq \left| \frac{G\Delta}{\tau_{des}} \right| [\text{mm}] \quad (2)$$

$$e \leq h_c \leq 3 \quad (3)$$

$$e \geq 6 \text{ mm} \quad (4)$$

$$h_c \leq 20 \text{ mm} \quad (5)$$

with h_c = width of the SG joint; e = thickness of the SG joint; a = short side dimension of the glass plane [mm]; w = relevant combined actions of wind, the snow, self-weight [MPa]; σ_{des} = design stress under tension [MPa]; Δ = maximum thermal movement—combined strains in both directions [mm]; G = shear modulus [MPa]; τ_{des} = design stress under shear [MPa]

$$\sigma_{des} = \frac{\sigma_k}{\gamma} [\text{MPa}] \quad (6)$$

with σ_k = characteristic breaking stress giving 75% confidence that 95% of the test results will be higher than this value [MPa]. γ = method or safety factor = 6

A pragmatic method that has become established and is frequently used in civil engineering is the material modeling of the SG joint using spring elements (Fachverband Konstruktiver Glasbau e.V. 21.09.21, Schuler et al. 2019; Descamps et al. 2020). This type of modeling brings several advantages to the practical application. The interaction between the adhesive joint and the global loadbearing structure can be modeled sufficiently precisely, efficiently, and clearly. In the case of large structures, it is impossible to idealize the joint with 3D FEM elements for all applications. The calculation effort increases immensely here, especially for different investigated joint properties. In addition, the high number of load combinations due to the combinatorics from (DIN EN 1990:2010-12) leads to an increase in calculation effort. However, the user must always be aware of the application's limits and

uncertainties. Due to the safety factors' magnitude, the bond's deformation behavior is only represented to a small extent. In addition, no conclusion can be drawn about the internal stress state of the bonded joint compared to modeling with 3D FEM elements.

When the modeling is performed using the idealization of the joint properties by structural springs, the linear adhesive joint is modeled using a series of force–displacement springs. The definitions of a joint section's spring elements are illustrated in Fig. 1a. The adhesive joint can be modeled with these spring elements defined, as shown in Fig. 1b. The supporting structure is modeled as a beam element, and glass pane with a shell element, and the SG-joint via springs with the distance Δ_F . Modeling with the structural spring elements ensures that the stiffness properties of the global model (shell and beam elements) and the connecting SG-joint can be considered in the same model and that interactions are captured during verification.

As an alternative, the analysis of the bonded joints can also be carried out with 3D FEM elements. This may become necessary as part of the design process if the application limits of the spring model can no longer be complied with or a more precise analysis of the internal stress in the joint is required. Appropriate procedures are described in (Fachverband Konstruktiver Glasbau e.V. 21.09.21, Maniatis et al. 2015; Drass and Kraus 2020a).

When modeling the SG joints with structural spring elements, the spring stiffness values are a decisive factor influencing the results of the structural calculation. According to (Fachverband Konstruktiver Glasbau e.V. 21.09.21), these stiffness values can be provided by adhesive manufacturers for joint dimensions within the specifications of the ETAG and according to (3–5).

Project-specific stiffness values must be determined experimentally for joint geometries deviating from the limits defined in (ETAG 002-1). Using the permissible stress σ_{des} , the effective joint modulus E_{joint} of the SG-joint is determined according to (7). σ_{des} can be calculated according to (6), where γ can be reduced to a factor of 4 with the permission of the adhesive manufacturer. Alternatively, σ_{des} can be taken from the ETA of the adhesive manufacturer. Exemplary values for the widely used bi-component structural silicone *DOWSIL™ 993* manufactured by *Dow* can be taken

Table 1 Material-properties of *DOWSIL™ 993*

Property			Source
$\sigma_{des,\gamma 6}$	[MPa]	0.14	$\gamma = 6$ according to (ETA-01/0005)
$\sigma_{des,\gamma 4}$	[MPa]	0.21	$\gamma = 4$ according to (Fachverband Konstruktiver Glasbau e.V. 21.09.21), when approved by the manufacturer
$\sigma_{k,ETA}$	[MPa]	0.84	Determined from σ_{des}
E_0	[MPa]	1.4	Elastic modulus in tension tangential to the origin – Dogbone test (ETA-01/0005)
E_{Young}	[MPa]	1.95–2.3	(Descamps and Hayez 2018) (Descamps et al. 2017)
E_{joint}	[MPa]	4.1	Joint modulus at origin for $12 \times 12 \text{ mm}^2$ SG joints (Descamps and Hayez 2018)

from Table 1.

$$E_{joint} = \frac{\sigma_{des}}{\epsilon_{des}} [\text{MPa}] \quad (7)$$

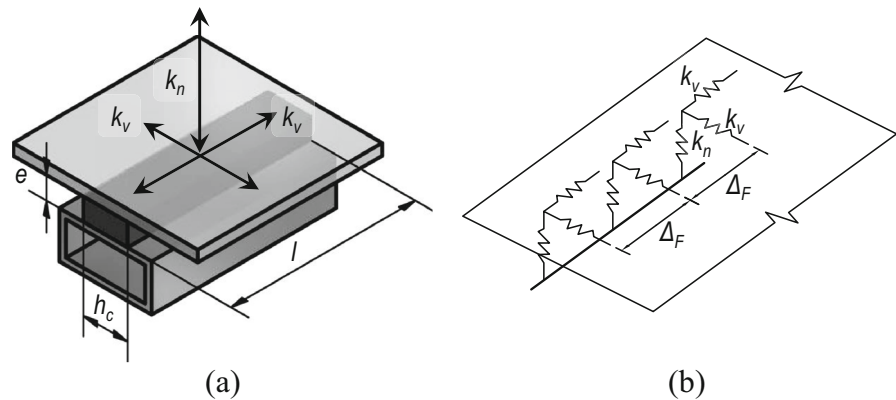
with E_{joint} = Effective modulus of the SG-joint (joint modulus) [MPa]; σ_{des} = permissible stress [MPa]; ϵ_{des} = strain at permissible stress [–].

As an alternative, the determination of the joint modulus E_{joint} of H-specimen under tensile load can also be performed using a rigidity factor $f_{rigidity}$ according to (Descamps et al. 2017). The rigidity factor $f_{rigidity}$ can be calculated from the aspect ratio h_c/e according to Eq. (8) for the investigated SG silicone *DOWSIL™ 993*. This relation can differ for other adhesives depending on the adhesive type and the Poisson ratio (Feynman et al. 2010). With this $f_{rigidity}$, the effective joint modulus E_{joint} can be calculated based on the young modulus of the adhesive under uniaxial tension E_{Young} , that is not influenced by the joint geometry, via Eq. (9) (Descamps and Hayez 2018; Descamps et al. 2020).

$$f_{rigidity} = 0.5743 * h_c/e + 1.52[-] \quad (8)$$

$$E_{joint} = f_{rigidity} * E_{Young} [\text{MPa}] \quad (9)$$

Fig. 1 Idealization of a joint section by structural spring elements: **a** definition of the spring elements of a joint section; **b** illustration of a model of an SG-joint between supporting structure and glass pane



with f_{rigidity} = rigidity factor [-]; E_{Young} = Young modulus of the adhesive under uniaxial tension [MPa].

With E_{joint} , the tensile stiffness for the structural spring element k_N can be calculated with Eq. (10) according to (Fachverband Konstruktiver Glasbau e.V. 21.09.21). The shear stiffness for the structural spring k_V is calculated accordingly with the joint shear modulus G_{joint} .

$$k_N = \frac{E_{\text{joint}} * A}{e} \left[\frac{\text{N}}{\text{mm}} \right] \quad (10)$$

with k_N = Tensile stiffness of the structural spring element [N/mm]; h_e = Width of the SG-joint [mm]; $A = h_e * \Delta_F$ = Area of the structural spring element [mm²]; e = Height of the SG-joint [mm].

Despite silicones being barely influenced by temperature thanks to their low glass transition temperatures (Habenicht 2009), typical influencing factors for plastics like (artificial) aging, the curing conditions, curing time, and the manufacturing process of the samples affect the properties of the SG joint. According to (ETAG 002-1), the initial mechanical strength test should be carried out with H-samples with a joint geometry of $12 \times 12 \times 50 \text{ mm}^3$ conditioned for 28 days after manufacturing at a temperature of $23 \pm 2 \text{ }^\circ\text{C}$ and $50 \pm 5\%$ relative humidity. (ETA-01/0005) defines a minimal time before transport of 21 days. Earlier transport may be allowed when the rupture is 100% cohesive and a minimal breaking stress of 0.7 MPa in the H-sample can be achieved.

The current SG guidelines do not define any specific methodology or guidance for manufacturing test specimens. For the determination of load-bearing properties, various parameters have an influence during and

after the manufacturing process. In this publication, the manufacturing process for modified H-samples in the style of (ETAG 002-1) is systematically investigated to minimize the interfering influences and to ensure an efficient determination of constant material properties. A systematically investigated and secured procedure to manufacture SG-specimen will be suggested. The aim is to make the sample production as economical as possible without compromising the test results.

The primary investigations aim to analyze the influence of the curing behavior of the specimens. The influence of different curing conditions on the properties is determined for specimens under tensile load. Various parameters such as specimen age, strength, stiffness, and failure pattern are checked for two different joint geometries to compare the curing methods. Depending on the curing method, a minimum specimen age is determined from which no relevant influence can be expected from the curing. The calculation methods used in practice, like the structural spring method, require material parameters that represent the load-bearing behavior to be applied. Therefore, suggestions are made for statistically validated strength and stiffness parameters for different curing conditions.

2 Experimental investigations

2.1 Method and specimen manufacturing

2.1.1 Definition of joint dimensions

The general shape of the modified H-specimen is based on the specifications in (ETAG 002-1) and was developed by (Schuler et al. 2017; Bues et al. 2019; Bues

Table 2 Joint geometries of the investigated modified H-specimens

Geometry [mm ²]	Joint dimensions		
	Height e [mm]	Width h_c [mm]	Length l [mm]
12 × 12	12	12	100
8 × 24	8	24	100

2021). Besides the standard geometry of 12 × 12 mm², an additional joint geometry of 8 × 24 mm² is investigated representing the limit value $h_e/e \leq 3$, to apply the calculation method in accordance with (ETAG 002-1) or the spring model in accordance with (Fachverband Konstruktiver Glasbau e.V. 21.09.21) without further stiffness investigations. The width of the joint h_c slightly exceeds the limit of $h_c \leq 20\text{mm}$ according to (ETAG 002-1). The length l of the modified H-specimen is increased from 50 to 100 mm compared to the ETAG H-specimen geometry to reproduce the behavior of a continuous joint more precisely (Schuler et al. 2017; Bues et al. 2019). The investigated geometries are summarized in Table 2.

2.1.2 Material and surface preparation

When designing specimens according to (ETAG 002-1), the exact material specifications used in the project and the surface preparation products must be used for the specimen. Two T-profiles (T 50 × 50 × 5 mm³) were used as a support profile to provide a rigid load path to the adhesive for the modified H-specimen used for these investigations. The rigid connection between the specimen and the testing machine ensures that the results are not influenced by deformations in the test setup or slippage, especially in the initial part of the test part.

Natural extruded aluminum (EN AW 6060 T66) was selected due to better machinability and lower cost of materials in contrast to (Schuler et al. 2017), where stainless steel and float glass was used as substrate materials. Figure 2 shows the modified H-specimen in comparison to a standard H-specimen. Prior to bonding, the aluminum was cleaned and wipe-degreased

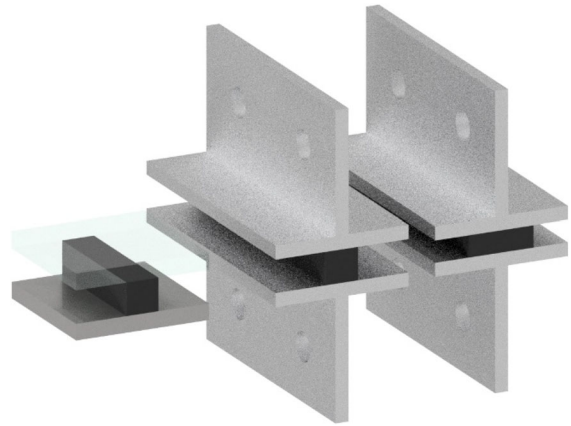


Fig. 2 H-specimen according to (ETAG 002-1) and mod-H-specimen with 12 × 12 mm² and 8 × 24 mm² joint ratio (left to right)

with isopropanol. After cleaning, the primer recommended by the adhesive manufacturer was used before applying the adhesive.

The influence of the surface treatment of the aluminum raised some uncertainties and was therefore investigated in preliminary studies. Next to the natural surface, the oxide layer was removed by a rough abrasive fleece with a comparable grain size of 180–220 before manufacturing. No relevant influence could be analyzed by the two surface pretreatments when analyzing the load-bearing behavior. All specimens showed similar stress–strain curves and a 100% cohesive failure, and no relevant difference in the failure pattern was detected.

Since the cohesive fracture pattern required in (ETAG 002-1) could also be determined in all further tests, as described in Sect. 2.3.5, it is assumed that the substrate surface has no relevant influence on the results of the load-bearing capacity tests shown here. Furthermore, it should be noted that the surface of the substrates can have a considerable impact when analyzing, for example, the artificial aging behavior of SG-adhesives or when planning real constructions. Here, only substrates are permitted to be used according to the manufacturer's specifications. The proposed way here seems reasonable in the interest of carrying out economically bearing capacity tests. For further examinations, the fracture pattern must continue to be consistently monitored to avoid influences. All specimens tested for this publication were manufactured with natural aluminum surfaces.

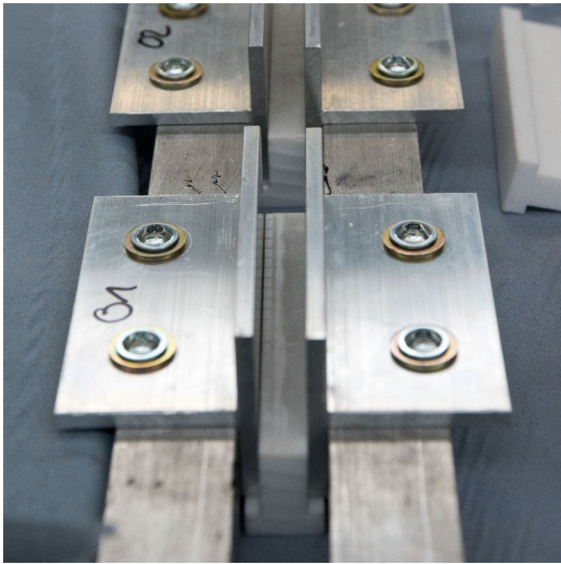


Fig. 3 Preparation of the T-profiles with plastic spacers on the bottom

2.1.3 Manufacturing

The specimens were manufactured under controlled laboratory conditions using a bi-component silicone material commonly used in the façade industry used for structural glazing systems. The adhesive was processed in an industry-standard mixing and dispensing system. Manufacturing took place at the company *seele* in Gersthofen, Germany.

Prior to the bonding process, the T-profiles were aligned perpendicular and fixed on mounting profiles. Plastic spacers manufactured out of polytetrafluoroethylene (PTFE) were placed under the T-profiles to achieve precise cross-section dimensions, as shown in Fig. 3. The joints were filled from the top from one side to the other with adhesive. After filling, the second plastic spacer was pushed into the gap, and the excess adhesive and air could escape to both sides. The two mounting profiles were clamped together with two clamps (Fig. 4) to secure the plastic spacers and get the precise height of the joint. After a minimum of 2 days of curing, the plastic spacers were removed, and the protruding ends of the adhesive were cut off with a sharp knife. The end of the finished specimen after cutting the protruded adhesive is shown in Fig. 5 for the two joint geometries.

Prior to testing, the real dimensions of the joint were measured with a digital caliper. All evaluations in this

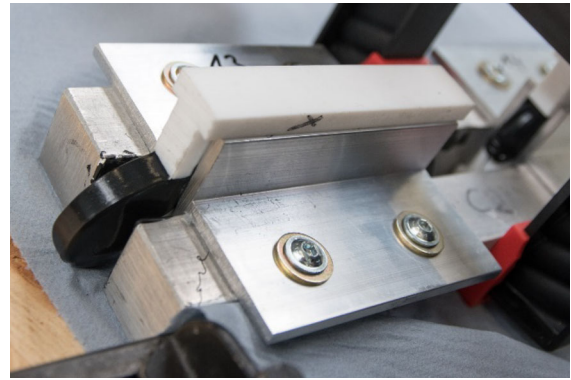


Fig. 4 Clamped and finished specimen with excess adhesive and two plastic spacers

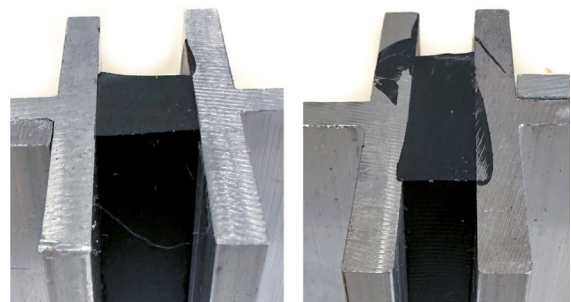


Fig. 5 End of the finished specimen after cutting the protruded adhesive

publication are based on real dimensions to avoid overestimating the adhesive's load-bearing capacity.

2.1.4 Methods for investigation of the manufacturing and curing influence

In preliminary tests, various parameters of the manufacturing process were analyzed and compared. Based on these investigations concerning the surface preparation of the aluminum profiles, the used material of the plastic spacers, and the dimensional accuracy of the joint cross-sections, the basis for the primary experimental investigations was established.

Curing conditions at room temperature (RT) can be defined as the standard method for SG adhesives. In addition, tempering at + 40 °C in a heating cabinet was selected as an alternative method, as storage at increased temperature was found to have a decisive influence on the load-bearing behavior of tensile-stressed H specimens. According to the Arrhenius equation, describing the kinetics of chemical reactions,

Table 3 Methods for specimen curing

Method	Pre curing [days]	Temper-ing 40 °C [days]	Post curing [days]	Total age at testing [days]
RT	7			7
	14			14
	21			21
40 °C (40)	7	6	1	14
	7	13	1	21
40 °C + RT (40+)	7	6	8	21
	7	13	8	28

Table 4 Test matrix with production batch for the curing behavior

Geometry [mm ²]	RT			40		40+	
	7d	14d	21d	14d	21d	21d	28d
12 × 12	I/II	I	I	I	I	II	II
8 × 24	I		II	II	II	II	

the rate of chemical reaction increases with the temperature. With every 10 °C increase in temperature, the chemical reaction rate approximately doubles (Gent 2012) according to a rule of thumb. No harmful influence is expected by this environmental condition, as the maximum processing temperature is in this range and according to (Schuler et al. 2017). All specimens were pre-cured for 7 days at RT before tempering them in the heating cabinet to generate a fundamental strength. The plastic spacers were removed during this time, and the excess adhesive was cut off. Besides the fundamental strength needed for better specimen handling, immediate tempering could generate bubbles during curing.

Generally, all specimens stored at RT were tested 7, 14, and 21 days after manufacturing. For the curing method “40” at the higher temperature, the samples were tempered for 6 and 13 days. After tempering, the specimens were post-cured for 1 day at RT to recondition. A total age at testing of 14 and 21 days is reached. To analyze the influence of being stored at RT for longer after tempering, the samples cured with the method “40+” were post-cured for 8 days and tested with a specimen age of 21 and 28 days. Table 3 summarizes the investigated curing methods. All methods were tested with the standard joint geometry of 12 × 12 mm². Furthermore, multiple curing conditions were selected for testing with the 8 × 24 mm² joint geometry of the modified H-specimen. For each test series

with the same parameters investigated, 6 samples were manufactured and tested.

All samples for investigating the effect of the curing condition on the properties of SG joints were manufactured in two production batches (I and II) with two different charges of SG silicone used. All other parameters relevant to production were changed as little as possible.

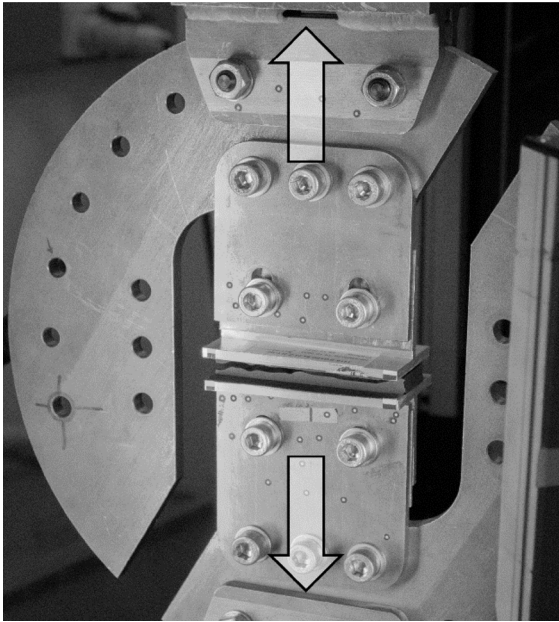
The initial reference properties of curing at RT for 7 days were produced two times with the two different charges of SG silicon to obtain an additional indication of the variance between the two manufacturing batches. An overview of the investigations carried out, including the production batch, can be found in the experimental matrix in Table 4.

2.2 Testing

All modified H-specimen were tested under global tensile load, related to a load acting at a 90° angle to the joint. The tests were carried out in a 100 kN universal testing machine, “Instron 5982”, with an interposed 10 kN load cell under displacement control. The load rate was selected according to (ETAG 002-1) with 5.0 mm/min for the joint with a height of 12 mm. The displacement rate here was 3.3 mm/min to maintain the strain rate for the 8 mm joint. Strain and load rates for

Table 5 Loading and strain rates

Geometry [mm ²]	Joint thickness [mm]	Displacement rate [mm/min]	Strain rate [1/min]
12 × 12	12 mm	5.0	0.42
8 × 24	8 mm	3.3	0.42

**Fig. 6** Test setup with load application structure, test specimen, and load direction

the tested joint dimensions are listed in Table 5. The test samples were mounted with screws in a rigid testing device manufactured from 10 mm thick steel. The displacement was measured with the deformation of the crosshead of the testing machine. Additionally, the displacement was recorded contactless on both sides of the sample with the video extensometer “RTSS” by “LIMESS Messtechnik u. Software GmbH.” The test setup is displayed in Fig. 6.

The difference between the crosshead travel and the video extensometer signals was analyzed by calculating the error over the entire test. Due to the rigid test setup and mounting of the samples, no relevant deviation was detected. The crosshead travel of the testing machine thus corresponds to the actual deformation of the adhesive. The further analysis performed in this

publication, particularly the strain calculation, is carried out with the traverse signal of the testing machine.

2.3 Curing influences

2.3.1 Overview

For analyzing the curing behavior of SG joints, stress–strain curves of the experimental tests will be compared. The stresses and strains were calculated using linear continuum mechanics of materials. The stress–strain behavior results from the load–deformation curve recorded during the test procedure. All graphs contain the nominal engineering stresses and strains. No conversion to true stresses and strains was performed. All following figures are scaled with the same axis limits for better comparability. For readability, only one representative curve per series is illustrated in color. The remaining curves are shown in light gray but with the same line type to show the variance in the series.

2.3.2 Specimen age

The stress–strain curves of the specimens with 12 × 12 mm² joint geometry cured at RT are shown in Fig. 7a. Considering the load-bearing behavior, the highest stiffness is for all series at the beginning of the experiment. From about 0.2 MPa stress, the stress–strain-curve flattens noticeably. Unlike this similarity, the four series tested can be aggregated into two groups with similar characteristics. The 6 specimens with an age of 21 days had higher stiffness and the ultimate fracture stress σ_{ult} exceeded that of the other group. After reaching the maximum stress, all specimens fail entirely in a very abrupt and brittle manner. In contrast, in the samples with a lower adhesive age of 7 and 14 days, the curve flattened at about 50% tensile strain, and the samples slowly started to fail. The final rupture started inconsistently at strains from 150 to over 250%. The variation of the ultimate fracture stress σ_{ult} is higher compared with the specimens with an age of 21 days.

The samples with an adhesive age of 7 and 14 days had similar adhesive properties that could be characterized by a lower fracture stress σ_{ult} and lower stiffness. A significant change in adhesive properties was observed when the age of 21 days was reached. It

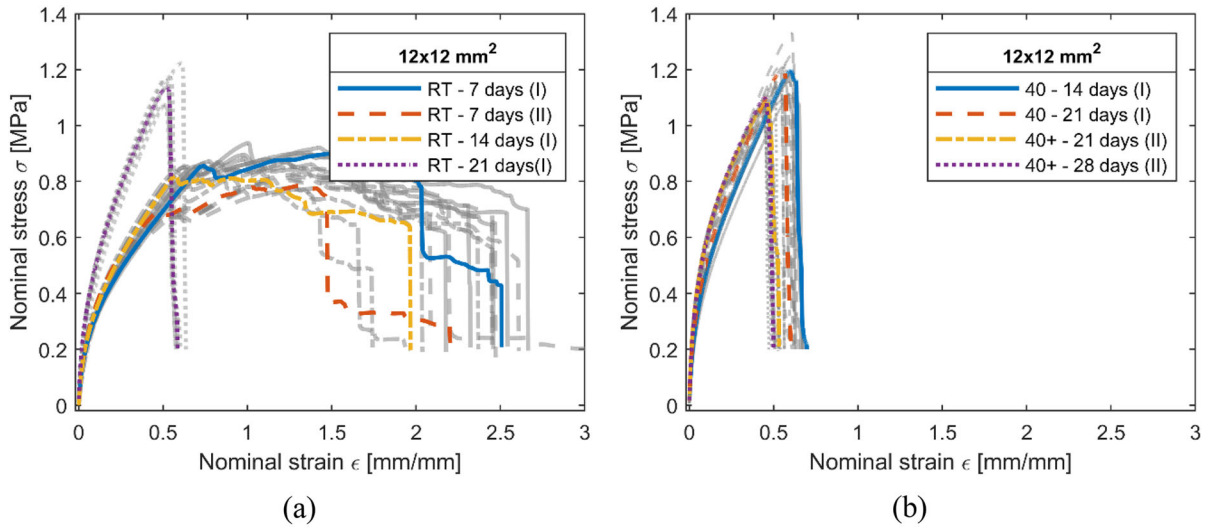


Fig. 7 Stress–strain curves: $12 \times 12 \text{ mm}^2$ joint geometry: **a** curing at RT; **b** curing at $40 \text{ }^\circ\text{C}$

appears that here the final adhesive properties were reached. Whether this statement can be confirmed will be verified in the following.

Samples with a specimen age of 7 days were manufactured and tested for the first (I) and the second (II) batch to investigate the influence of different production batches. Here, all samples of the second batch failed at a significantly lower ultimate stress σ_{ult} compared to the specimen of the first series. As both series were produced under the same controlled manufacturing conditions apart from the two charges of SG silicone used, this difference may be caused by this. These fluctuations were unavoidable, as only a limited number of samples could be tested and manufactured simultaneously and must be considered in the subsequent interpretation of the various influences. The load-bearing behavior of the specimens with an adhesive age of 7 and 14 days is very similar. From an engineering point of view, it was expected that this series' properties would be between those of the 7 and 21 days old samples.

2.3.3 Curing method

After curing at $40 \text{ }^\circ\text{C}$, all series with joint geometries of $12 \times 12 \text{ mm}^2$ behaved rather similarly, as shown in Fig. 7b. The load-bearing and failure behavior of all curves fitted well with those of the samples cured at RT for 21 days, as shown in Fig. 8. The two series stored for one week at RT after curing at $40 \text{ }^\circ\text{C}$ ($40 + \text{ }^\circ\text{C}$) failed at minimal lower ultimate fracture stresses σ_{ult} . When

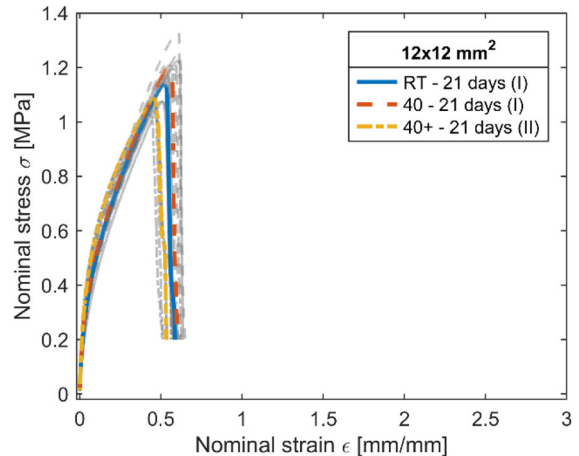


Fig. 8 Stress–strain curves: $12 \times 12 \text{ mm}^2$ joint geometry curing for 21 days at RT and $40 \text{ }^\circ\text{C}$

interpreting this effect from an engineering point of view, the strength of the specimens should not decrease due to extended storage at room or higher temperature. Investigations by (Schuler et al. 2017) show that negative effects on single lap joints and H-specimens could be observed by heat storage up to $95 \text{ }^\circ\text{C}$. The production influences, due to two different charges of SG-silicone used, might explain the reduction in strength. The decrease in ultimate fracture stresses σ_{ult} was in a very similar proportion compared to the two reference series with 7 days old specimens at RT.

Overall, the scatter in the specimens cured at a controlled temperature of 40 °C appears reasonable, especially if considering production-related irregularities in preparing component-like samples cannot be avoided.

2.3.4 Geometry

The influence of the joint geometry on the load-bearing behavior was investigated in (Bues 2021). The influences determined due to the variation of the joint geometry can be confirmed by these investigations, especially for the load-bearing behavior of the tempered specimens.

The joints with the higher ratio h_e/e of 3 showed a stiffer stress–strain curve than the joints with a ratio of 1. Similar to the narrower joints, the stiffness dropped slightly at a stress of 0.2 MPa. The failure behavior of the two geometries was also comparable. For the specimens with an age of 7 days at RT, the stress–strain curve flattened nearly completely after reaching its maximum stress. The complete failure of the joints with a geometry of $8 \times 24 \text{ mm}^2$ occurred with an elongation of about 350%. These results are shown in Fig. 9a for samples cured at RT for 7 days and 40 + °C for 21 days.

Regarding the ultimate fracture stress σ_{ult} , no relevant difference could be detected between the two joint geometries. The increase in strength due to tempering at 40 °C was in a similar range. The stiffness for the $12 \times 12 \text{ mm}^2$ joint cured for 21 days at 40 + °C was comparable with the $8 \times 24 \text{ mm}^2$ joints cured for 7 days at RT.

To compare the influence of tempering methods on $8 \times 24 \text{ mm}^2$ joint geometry, the stress–strain curves of 4 test series with a specimen age of a minimum of 14 days are shown in Fig. 9b. All series had a similar stiffness behavior at the beginning of the experiment, with a minimally increased stiffness of the two series cured at 40 °C and 40 + °C for 21 days. Like all other observed stress–strain curves, a first minor drop in stiffness was observable at about 0.2 MPa. At about 15% tensile strain, all curves flatten out visibly until the final rupture occurs. The final fracture happens at a nominal tensile strain between 25 and 30%, except for the series cured at RT, where the drop in stress occurs from 40 to 50% strain. The ultimate fracture stress σ_{ult} is nearly the same for 3 test series. Only the one tested

after curing at 40 °C for 14 days fails at minimal lower values.

After reaching the final adhesive properties, no relevant influence of the specimen age and the curing method on the load-bearing behavior of the tested joints could be detected. The minimum required specimen age for expecting the final adhesive properties depended on the geometry and the curing method. In chapter 2, the effect of the curing conditions and adhesive age on mechanical strength and stiffness properties will be investigated in more detail. Table 6 summarizes the required minimum specimen age for expecting the final strength properties.

2.3.5 Failure pattern

After the tests, all samples' failure patterns were photographed and shown for four exemplary samples in Fig. 10. Within the repeats with the same curing condition, the fracture patterns did not deviate relevantly from each other.

In addition to the influence due to the different joint geometries, differences in the fracture patterns could also be detected due to curing. For the $12 \times 12 \text{ mm}^2$ joint after 7 days of curing at RT, shown in Fig. 10a, the failure pattern is characterized by two different areas. The white dotted line indicates the transition of the two patterns. A rather rough pattern on the outside changes to a wavy pattern on the inside. The pattern with two areas disappeared at the specimen cured for 21 days at 40 °C, as in Fig. 10b. A relatively uniform pattern with small waves formed over the entire fracture surface. This failure pattern from Fig. 10b is also characteristic for the specimen cured at RT for 21 days.

For the larger joint geometry of $8 \times 24 \text{ mm}^2$ displayed in Fig. 10c after curing for 7 days at RT, the failure pattern can be characterized by three areas. A similar failure pattern can be observed compared to Fig. 11a in the outer part of the adhesive area. The transition to a rough wavy pattern on the inside is indicated by with dotted white line. In the middle of the adhesive, the third area of the pattern can be noticed in contrast to the $12 \times 12 \text{ mm}^2$ joint geometry. The dot-dashed line highlights the transition.

For the pattern in Fig. 10d, three areas can still characterize the failure pattern after curing for 21 days at 40 + °C. The outer one is located outside of the dot-

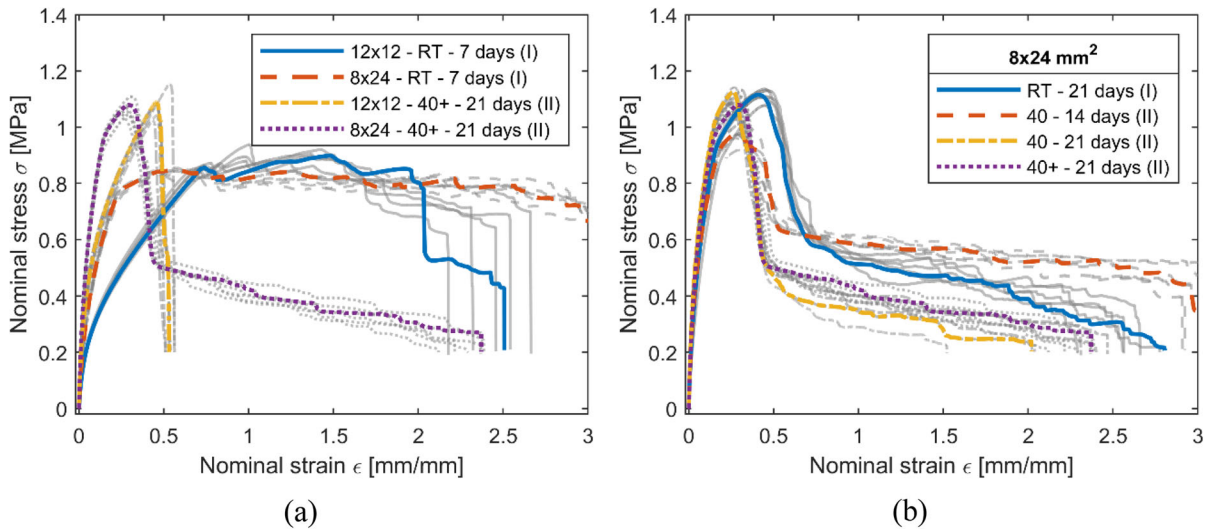


Fig. 9 Stress–strain curves: **a** 12×12 and 8×24 joint geometry after different curing conditions; **b** $8 \times 24 \text{ mm}^2$ joint geometry

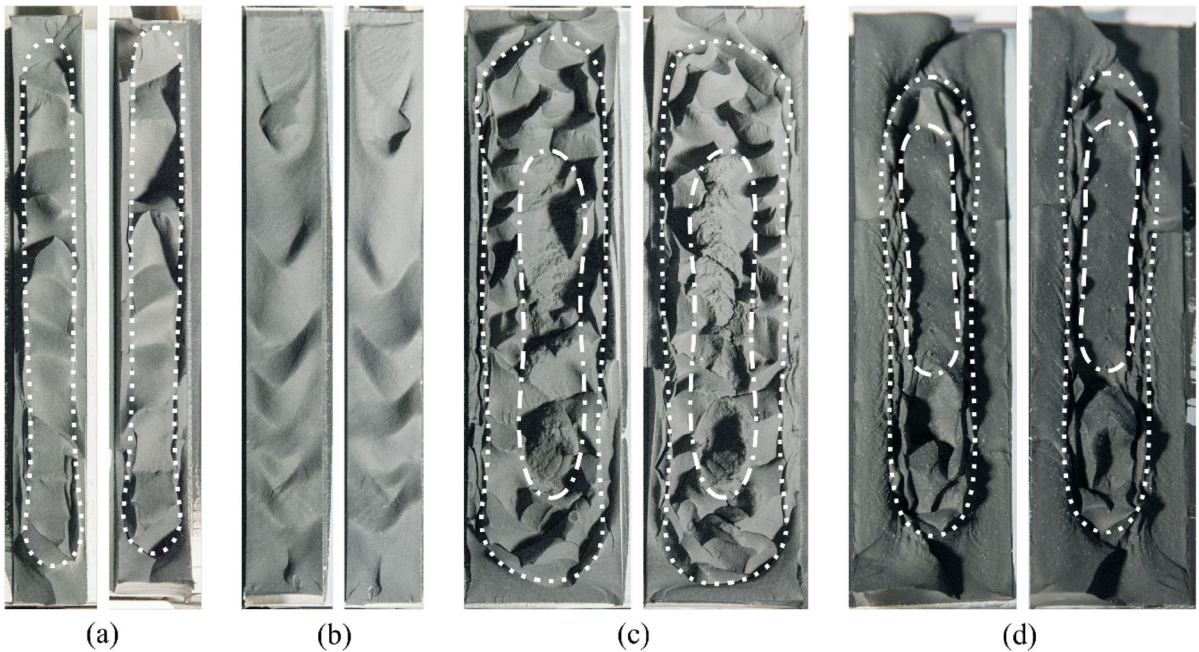


Fig. 10 Exemplary failure pattern for different geometries and curing conditions: **a** $12 \times 12 \text{ mm}^2$, 7 days at RT; **b** $12 \times 12 \text{ mm}^2$, 21 days at $40 \text{ }^\circ\text{C}$; **c** $8 \times 24 \text{ mm}^2$, 7 days at RT; **d** $8 \times 24 \text{ mm}^2$, 21 days at $40+ \text{ }^\circ\text{C}$

ted line increased. Here, the pattern changed to a relatively smooth pattern. Inside the ring, the rough pattern between the two lines remains visible. The pat-

tern inside the dash-dotted line changed to a smooth surface. Only a few tiny bubbles with a diameter from about 0.5–1.0 mm can be detected here.

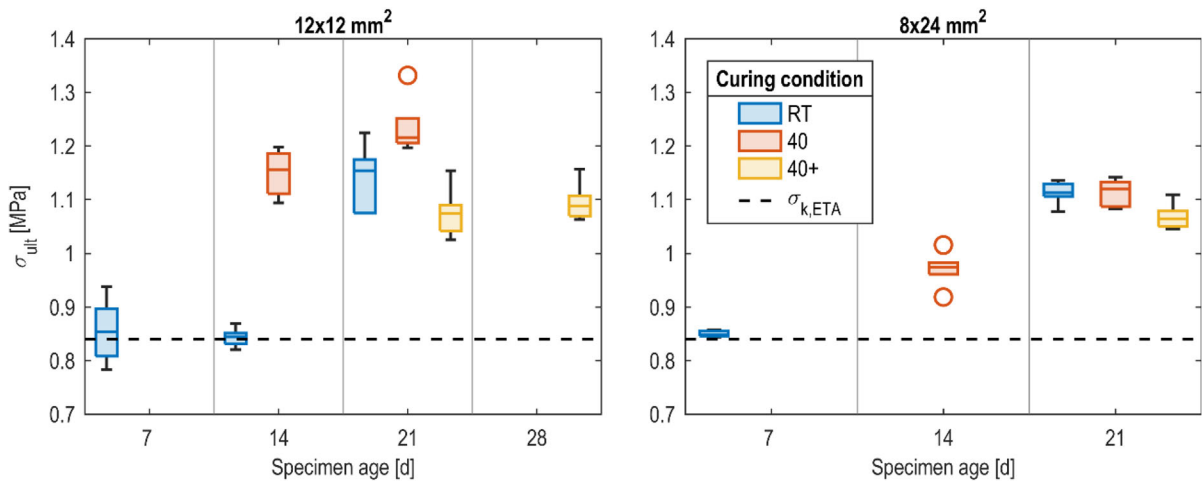


Fig. 11 Ultimate fracture stress σ_{ult} depending on the age of the specimen and the curing conditions

3 Proposal of joint properties for tensile specimen

3.1 Initial mechanical strength

3.1.1 Definition of the mechanical strength properties

For further investigating and comparing the influence of tempering on the properties of SG joints under tensile load, characteristic parameters for the strength and stiffness of the specimens were determined from the stress–strain curves.

According to (ETAG 002-1), the initial mechanical strength is represented as the average ultimate breaking stress σ_{ult} from all samples. To perform a general statistical interpretation, the characteristic breaking stress σ_k defined as the 75% confidence interval of the 95% quantile of the test results can be calculated with Eq. (11). The determination of the fractile factor k_3 requires the application of the noncentral student’s t distribution with a non-centrality parameter δ (Beech and Owen 1962; Loch 2014). For practical application, values for the k_3 factors are given in (ETAG 002-1, ISO 16269-6:2014-01). Within the scope of this publication, the calculation of the characteristic breaking stress σ_k was carried out using the method according to (ETAG 002-1). In this way, the best possible comparability with the manufacturer’s value $\sigma_{k,ETA}$ is ensured.

$$\sigma_k = \bar{x}_{\sigma_{ult}} - k_3(n, p, 1 - \alpha) \times \bar{s} [\text{MPa}] \quad (11)$$

with σ_k = the characteristic breaking stress (75% confidence that 95% of the test results will be higher than this value [MPa]; $\bar{x}_{\sigma_{ult}}$ = arithmetic mean of σ_{ult} [MPa]; $k_3(n, p, 1 - \alpha)$ = Fractile factor for characteristic values [-]; n = Sample size [-]; p = P-quantile value [-]; $1 - \alpha$ = Confidence level [-]; \bar{s} = Standard deviation of the series under consideration [MPa].

As can be seen from Eq. (11), the fractile factor k_3 is directly influenced by the number of specimens when determining σ_k . The influence of the variance of the samples is thus weighted more strongly with less samples. The mean value $\bar{x}_{\sigma_{ult}}$ is only indirectly influenced by the number of samples. For the general analysis of the various influencing factors, the use of the arithmetic mean $\bar{x}_{\sigma_{ult}}$ or the median of the ultimate breaking stress σ_{ult} has proven to be advantageous. Boxplot diagrams are a standard tool in descriptive statistics to visualize the median and the variance. The top and bottom of the box represent the 25% and 75% quantiles, and the height of the box is the interquartile range (IQR). The line inside the box corresponds with the median value. Outliers are detected when their position is more than $1.5 \cdot \text{IQR}$ from the box. The lines above and below each box, called whiskers, connect to the box with the maximum value that is not an outlier (The Mathworks, Inc. 2022).

Especially with many data points, these statistical parameters can be displayed clearly, and an easy comparison is possible. With a minimum of 6 data points per series, the application of this diagram is possible, but the interpretation is less straightforward compared to

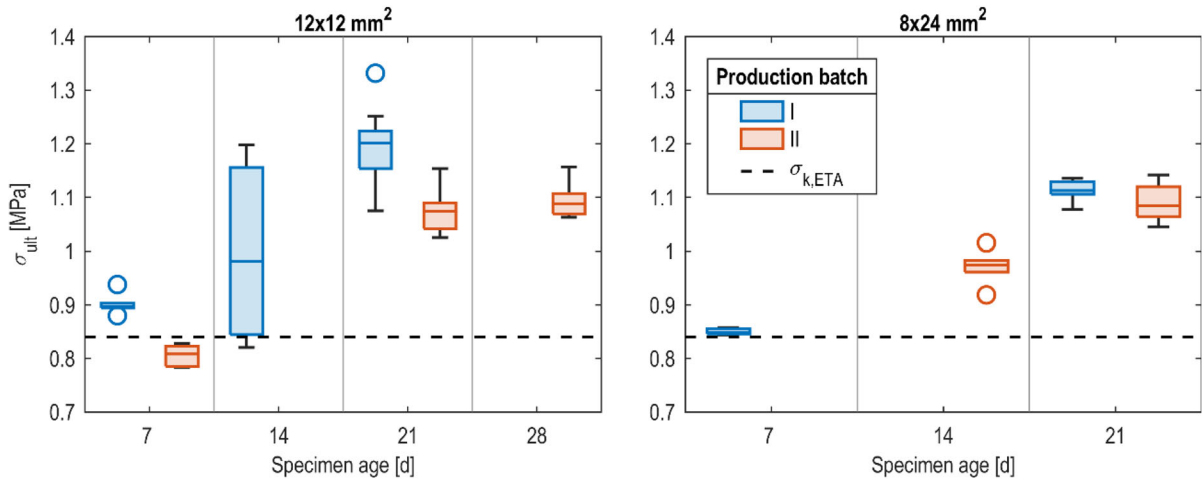


Fig. 12 Ultimate fracture stress σ_{ult} depending on the age of the specimen and the production batch

extensive data series. Despite this, an excellent description of the measured values by the median and the variation is possible with the boxplot diagram. In addition, with the help of the grouped boxplot diagrams, the classification of data with two variables is possible, and a good understanding of the data can be achieved.

After analyzing the various influencing factors, the samples are regrouped, and a statistical evaluation is performed. A comparison with the characteristic breaking stress $\sigma_{k,ETA}$ from Table 1 given by the adhesive manufacturer is therefore possible.

3.1.2 Analysis of the mechanical strength

Figure 11 shows the ultimate fracture stress σ_{ult} separated for the $12 \times 12 \text{ mm}^2$ as well as the $8 \times 24 \text{ mm}^2$ joint geometry. The individual diagrams are categorized by specimen age as well as curing method. For the $12 \times 12 \text{ mm}^2$ joint, two separated groups become visible. One group shows a lower ultimate stress σ_{ult} in the range of σ_k . The second group can be characterized by a significantly higher fracture stress σ_{ult} of over 1 MPa. In addition to all samples with an age of a minimum of 21 days, this higher strength can also be achieved by the samples with an age of 14 days after curing at 40°C . In contrast, the series with an age of 14 days is located between the two groups for the wider geometry. It can thus be assumed that a slightly longer curing time of a minimum of 21 days is required for the wider geometry, which is independent of the curing method used. This effect can be explained, as in wider

joint geometries, any potential by-products developed during the curing process needs more time to leave the specimen.

In Fig. 12, the same data is categorized by the production batch instead of the curing method, where a significant influence of the manufacturing batch can be detected. Comparing the scatter of the data groups with a specimen age of 21 days or higher, this influence of the curing method is similar to that of the production batch. For the specimens with an age of a minimum of 21 days, it can be assumed that the influence of the curing conditions on the strength can instead be attributed to the differences from the production batches and, therefore, two different charges of SG-silicone used. After reaching the final strength properties, no change in the ultimate stress σ_{ult} can be detected due to further storage.

To investigate the influence of the curing condition in more detail and to reduce the influence of the production series, the ultimate stress σ_{ult} is related to the initial mean ultimate stress of the $12 \times 12 \text{ mm}^2$ joint $\sigma_{ult \text{ mean } 7d}$. The result is shown in the scatter plot in Fig. 13. Random values in the range of ± 1 day are added to the specimen age to increase the readability of the diagram. The corresponding production batch is represented by the marker type, and the curing condition by the marker color. With these results, it becomes evident that for both joint geometries, the specimen cured at RT for 21 days does not yet wholly reach the strength of the specimen cured at 40 or 40+. The means of the normalized ultimate stress $\sigma_{ult}/\sigma_{ult \text{ mean } 7d}$ from

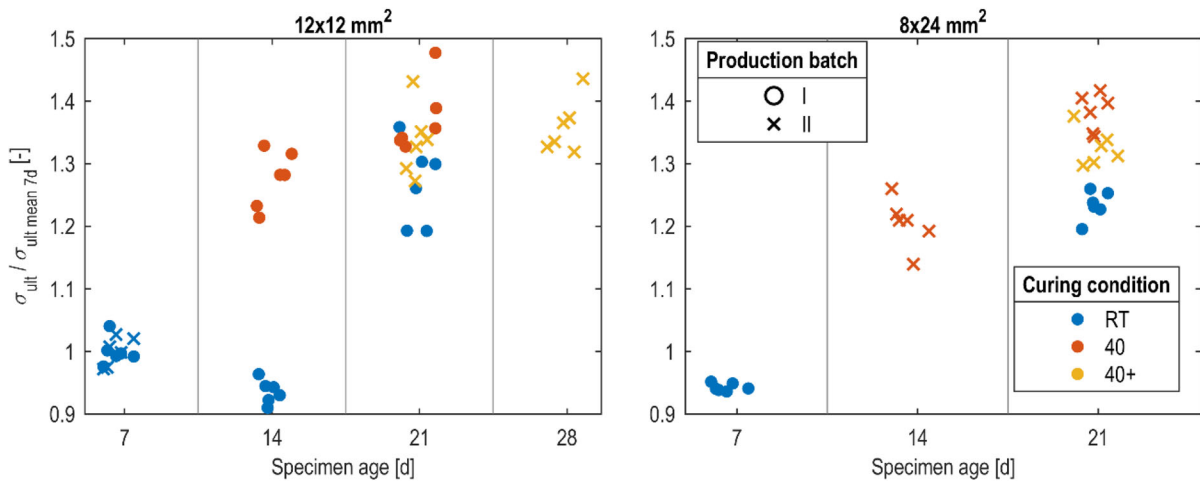


Fig. 13 Related ultimate fracture stress σ_{ult} depending on the age of the specimen and the production batch

the specimens cured at RT differ significantly from those cured with method 40. After 21 days and curing at 40, the highest ultimate stress σ_{ult} could be achieved.

In summary, it can be confirmed that the tempering method and specimen age influence the strength properties of the specimens. After the final properties have been reached, the differences are largely determined by the production batch, and the test date has only a minor influence. The $8 \times 24 \text{ mm}^2$ joint geometry shows smaller variations in ultimate stress σ_{ult} compared to the $12 \times 12 \text{ mm}^2$ joint geometry. The required minimum specimen age for expecting the final strength properties shown in Table 6 can be confirmed based on this chapter’s evaluation of the strength parameters. For the specimens with final strength properties, the ultimate stress σ_{ult} were achieved. In addition to the faster curing process, no negative aspects could be observed by tempering the specimen at 40°C and due to subsequent storage after tempering at 40+.

3.1.3 Statistical evaluation of the mechanical strength

All specimens are categorized into three groups to perform a statistical evaluation. The minimum specimen age for final material properties is defined in Table 6 as a function of the curing method. Initial properties are defined for all specimens tested after curing at RT for 7 days. All samples between the initial and final properties are categorized as intermediate (inter). Table 7 shows a statistical evaluation. Besides the mean, minimum (min), maximum (max) values, and the standard

Table 6 Required specimen age for final adhesive properties depending on the curing method and geometry

Geometry [mm ²]	Curing method	
	RT	40 °C
12 × 12	28 days	21 days
8 × 24	28 days	21 days

deviation (Std Dev), σ_k is calculated according to the procedure in Sect. 3.1.1.

For the $12 \times 12 \text{ mm}^2$ joint geometry, a relative difference of 30% between the mean values of the initial and final ultimate stress $\sigma_{ult,mean}$ can be observed. For the $8 \times 24 \text{ mm}^2$ joint, the increase is 28%. The characteristic breaking stress σ_k calculated for the specimen with initial properties and a joint geometry of $12 \times 12 \text{ mm}^2$ is affected by the high standard deviation due to the two production batches. For the $8 \times 24 \text{ mm}^2$ geometry, $\sigma_{ult,mean}$ and σ_k are nearly the same because of the low variance.

Regarding the characteristic breaking stress $\sigma_{k,ETA}$ from Table 1, which is given by the manufacturer in the ETA, the characteristic breaking stress σ_k calculated for the specimen with initial properties is slightly lower. σ_k of the samples with final properties exceeds $\sigma_{k,ETA}$ defined by the manufacturer by 16% for the $12 \times 12 \text{ mm}^2$. For the $8 \times 24 \text{ mm}^2$ joint geometry,

Table 7 Summarized statistical evaluation of the ultimate fracture stress σ_{ult} and σ_k

Geometry [mm ²]	Adhesive properties	Number of specimens	σ_{ult}				Std Dev	σ_k 95% quantile 75% probability
			Min	$\bar{x}_{\sigma_{ult}}$	Max			
			[MPa]	[MPa]	[MPa]	[MPa]	[MPa]	
12 × 12	Initial	12	0.78	0.85	0.94	0.05	0.75	
12 × 12	Inter	18	0.82	1.05	1.22	0.15	0.75	
12 × 12	Final	18	1.03	1.14	1.33	0.08	0.97	
8 × 24	Initial	6	0.84	0.85	0.86	0.01	0.84	
8 × 24	Inter	12	0.92	1.04	1.14	0.08	0.88	
8 × 24	Final	12	1.05	1.09	1.14	0.03	1.02	

an increase of 22% can be determined. For these values must be mentioned that the characteristic breaking stress σ_k for the 8 × 24 mm² geometry could only be calculated with specimens of the second production batch. From the first batch, no specimens with final properties were manufactured. Although the strength of the second batch is assumed to be slightly lower, the low variance leads to the high value of σ_k .

The tests presented here show that the values proposed by the manufacturers in the ETA are on the safe side. The exact size of the variation due to the different production batches can only be estimated approximately based on the small database and should be analyzed in more detail by further investigations.

3.2 Stiffness

3.2.1 Definition of the stiffness properties

To determine the stiffness parameters of SG joints, in (ETAG 002-1), the determination of a secant module at 12.5% strain on an H-specimen is proposed. The initial stiffness is subsequently used to analyze the influence of artificial aging on the stiffness properties.

The calculation based on a hyperelastic material model is suggested by (Descamps et al. 2017; Descamps and Hayez 2018) to determine the stiffness of an SG-joint. Depending on the aspect ratio h_c/e of the joint geometry, the effective joint module ranges from E_{young} for very low aspect ratios to a theoretical maximum value of approximately 17 times E_{young} . The relationship between the joint modulus E_{joint} and

the young modulus E_{young} of the joint can be expressed via Eq. (9), and the rigidity factor $f_{rigidity}$. To determine the rigidity factor $f_{rigidity}$, the stress–strain data of SG specimens with different aspect ratios were fitted to the neo-hookean relationship in Eq. (12) by a least-squares algorithm. The fitting is calculated up to 15% strain.

$$\sigma = f_{rigidity} G \left(1 + \varepsilon - \frac{1}{(1 + \varepsilon)^2} \right) \tag{12}$$

Alternatively, (ISO 527-1:2019) defines two methods for determining the young modulus of plastics. In addition to a strain-based determination of the secant modulus, a linear regression calculation is possible. The slope of the regression line is determined using the least squares method. For both methods, the defined strain range for the evaluation is between 0.05 and 0.25%.

According to (Fachverband Konstruktiver Glasbau e.V. 21.09.21), the stress–strain diagram of the joint can be used to calculate the joint modulus according to Eq. (7). The permissible stress σ_{des} can be calculated based on the used calculation method with the method factor $\gamma = 4$ or 6. In the following, σ_{des} is calculated with $\gamma = 4$, since this value is usually used when the structural spring model is applied.

When determining the joint modulus E_{joint} experimentally, it is practical to extend (7) to (13) according to (DIN EN ISO 527, Müller et al. 2023), so the secant modulus is determined in a previously defined stress or strain range. In this way, inevitably arising inaccuracies at the start of the experiment can be relatively

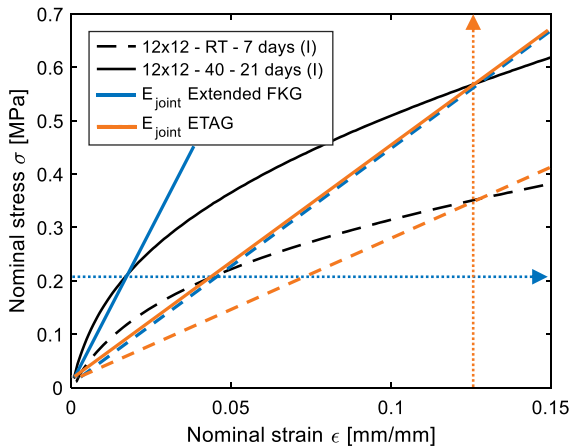


Fig. 14 Determination of the joint modulus E_{joint} with the extended FKG and the ETAG method

easily circumvented. In the investigations in this publication, σ_1 was selected as 0.02 MPa, as here, a good compromise between the accuracy of the joint modulus and inaccuracies due to the start of the experiment could be reached.

To adapt the defined strain range in (ISO 527-1:2019) to the low-modulus SG-silicones in (Müller et al. 2023), an adaption to the range of use of the adhesives via (14) may be possible. The methods available for determining joint stiffness are summarized in Table 8.

$$E_{joint} = \frac{\sigma_{des} - \sigma_1}{\epsilon_{des} - \epsilon_1} \tag{13}$$

With: $\sigma_1 / \epsilon_1 =$ stress/strain at the start of the secant modulus

$$\epsilon_{Ref} = \frac{\sigma_{des, \gamma 4}}{E_{joint}} = \frac{0.21 MPa}{4 MPa} = 0.0525[-] \tag{14}$$

In Müller et al. (2023), the influence of the evaluation method is investigated for the methods according to the extended FKG, the ISO 527-1 (adapted secant), and the ETAG 002-1. It could be shown that due to the hyperelastic material behavior, the chosen method has a relevant influence. Figure 14 shows an example of the determination of the joint modulus E_{joint} using two specimens with a joint geometry of $12 \times 12 \text{ mm}^2$ for the extended FKG and ETAG methods.

According to (Descamps and Hayez 2018), an evaluation method based on the hyperelastic material behavior represents an additional promising approach for representing higher strain ranges.

When calculating SG-joints in glass or facade elements with the presented structural spring elements, the load-bearing behavior of the joint up to a stress of $\sigma_{des} = 0.21 \text{ MPa}$ or approx. a strain of $\epsilon = 5.25\%$ is usually considered. Only a minor difference between linear or nonlinear regression was recognizable for analyzing the relatively small strain ranges. For this reason, the influence of manufacturing and curing effects on stiffness is analyzed with the extended FKG method within the scope of this publication.

3.2.2 Analysis of the stiffness

In Fig. 15, the joint modulus E_{joint} calculated with $\sigma_{des(4)}$ and $\gamma = 4$, is displayed separately for the two joint geometries. As in the previous chapter, the individual diagrams are categorized by specimen age and curing condition. The emergence of two outliers occurring at a specimen age of 21 days for both geometries cannot be explained with certainty. A combination of influences from production, curing, installation in the testing machine, and testing of the specimens can lead to this deviation.

A general correlation between the SG joint's stiffness and the specimen's age can be observed. With an increased specimen age, the joint modulus E_{joint} increases as well. For the specimen of the same age, an increase in stiffness can be observed by curing at the higher temperature. The increase in stiffness and further curing matches the Arrhenius equation, which describes the relationship between chemical reaction rate and temperature.

When analyzing the stiffness of the specimen with an age of 21 days and curing at 40 °C and 40+ °C, the significant difference in stiffness cannot be explained by the influence of the curing condition. Therefore, Fig. 16 shows the joint modulus E_{joint} categorized by the production batch instead of the tempering method. Here, for the specimen with the same age, a higher stiffness of the second production batch can be observed. Therefore, the previously mentioned difference between the two curing methods in Fig. 15 with a specimen age of 21 days can be explained. A similar effect can be observed for the specimen with a geometry of $8 \times 24 \text{ mm}^2$ and an age of 14 days, which seems to have a

Table 8 Methods for determining the stiffness of SG-joints

Method	Equation	Limits	Analysis principle	Source
FKG	$E_{joint} = \frac{\sigma_{des}}{\epsilon_{des}}$	$\sigma_{des} = 0.21 \text{ MPa}$	Stress based secant modulus	Fachverband Konstruktiver Glasbau e.V. 21.09.21
Extended-FKG	$E_{joint} = \frac{\sigma_{des} - \sigma_1}{\epsilon_{des} - \epsilon_1}$	$\sigma_{des} = 0.21 \text{ MPa}$ $\sigma_1 = 0.02 \text{ MPa}$	Stress based secant modulus	Müller et al. (2023)
ISO 527-1 (secant)	$E_{joint} = \frac{\sigma_2 - \sigma_1}{\epsilon_2 - \epsilon_1}$	$\epsilon_1 = 0.05\%$ $\epsilon_2 = 0.25\%$	Strain based secant modulus	(ISO 527-1:2019)
ISO 527-1 (regression)	$E_{joint} = \frac{\delta\sigma}{\delta\epsilon}$	$0.05\% \leq \epsilon \leq 0.25\%$	Strain based Linear regression	(ISO 527-1:2019)
ISO 527-1 (adapted secant)	$E_{joint} = \frac{\sigma_2 - \sigma_1}{\epsilon_{Ref} - \epsilon_1}$	$\epsilon_1 = 0.05\%$ $\epsilon_2 = 5.25\%$	Strain based secant modulus	Müller et al. (2023)
ETAG	$K_{12.5} = E_{joint} = \frac{\sigma}{\epsilon}$	$\epsilon = 12.5\%$	Strain based Secant modulus	(ETAG 002-1)
Rigidity factor	$E_{joint} = f_{rigidity} * E_{Young}$	$\epsilon \leq 15\%$	Strain based Nonlinear regression	Descamps et al. (2017)

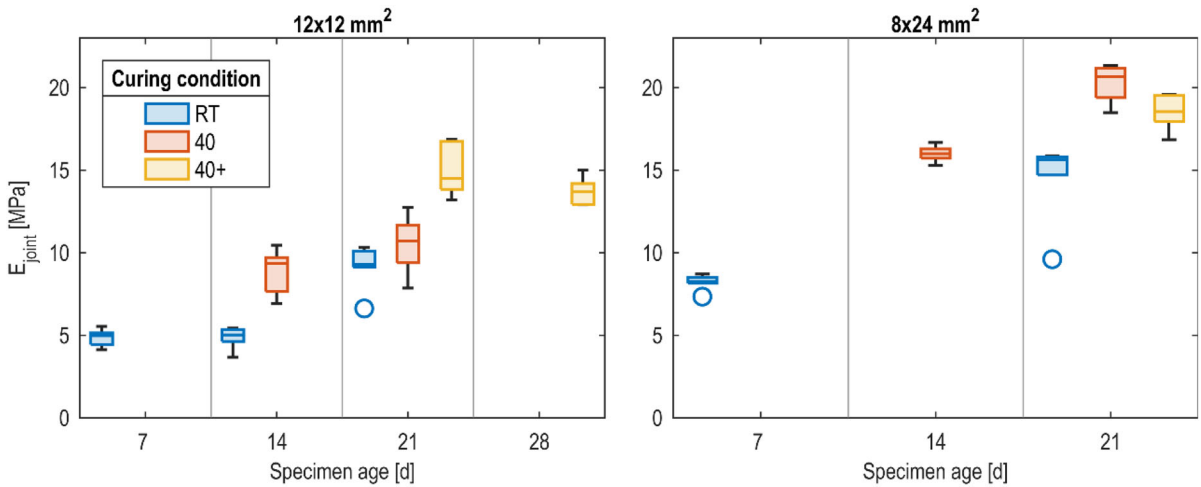


Fig. 15 Joint modulus E_{joint} depending on the age of the specimen and the curing conditions

similar stiffness to the samples with an age of 21 days. Here, the relatively high stiffness of the 14-day-old samples may also be explained due to the production batch.

To investigate the influence of the curing condition in more detail and to reduce the influence of the production series, the joint modulus E_{joint} is related to the initial mean joint modulus of the $12 \times 12 \text{ mm}^2$ joint $E_{joint \text{ mean } 7d}$. The result is shown in the scatter plot in Fig. 17. To increase the readability of the diagram, a

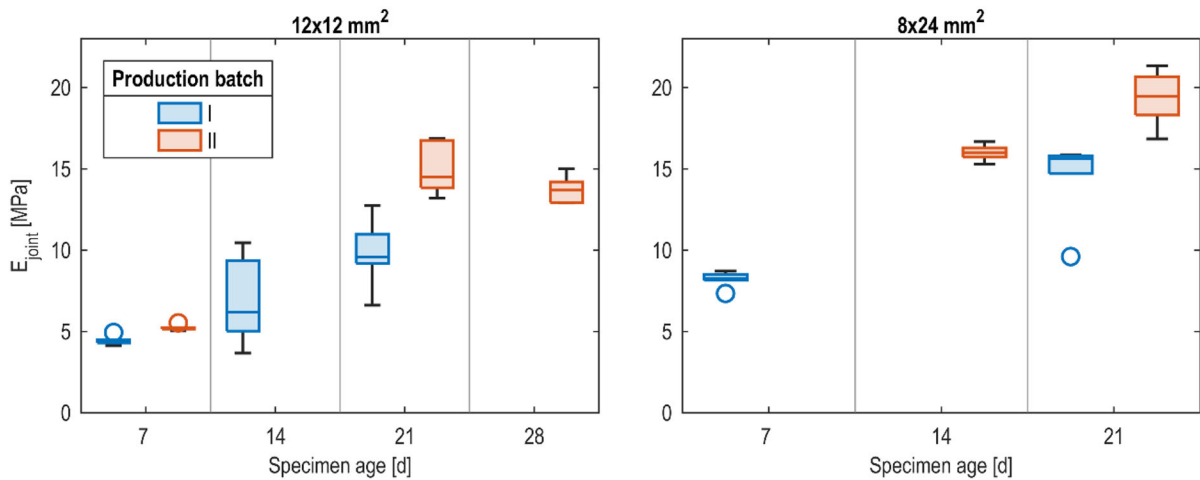


Fig. 16 Joint modulus E_{joint} depending on the age of the specimen and the production batch

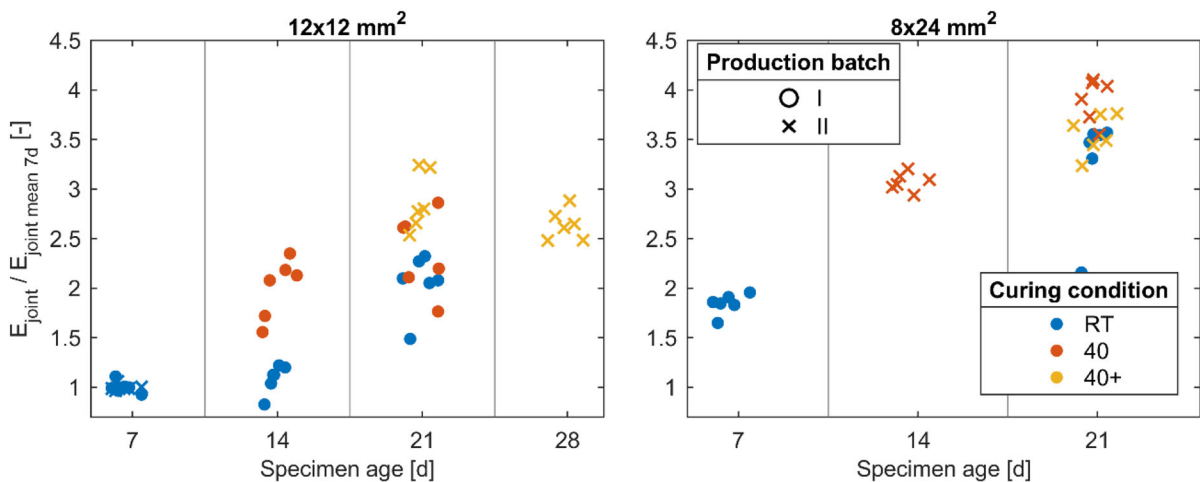


Fig. 17 Related joint modulus E_{joint} depending on the age of the specimen and the production batch

random scatter with ± 1 day is added to the values of the specimen age. The corresponding production batch is represented by the marker type, and the curing condition by the marker color. With these results, it becomes evident that for both joint geometries, the specimen cured at RT for 21 days nearly reaches the stiffness of the specimen cured at 40 or 40 + . The specimen with the $12 \times 12 \text{ mm}^2$ joint geometry shows a larger scatter than the $8 \times 24 \text{ mm}^2$ joint. After 21 days and curing at 40 or 40 + , the highest values of the joint modulus E_{joint} could be achieved.

3.2.3 Statistical evaluation of the mechanical strength

Compared to the strength parameters of the joints, the stiffness parameters change much more consistently over the specimen age. When trying to divide the results into groups with initial, intermediate, and final joint parameters, a similar division as defined in Table 6 for the ultimate stress σ_{ult} seems suitable.

To compare initial and final stiffness parameters, Table 9 shows a statistical evaluation. Comparing the mean joint modulus E_{joint} of the specimen with initial and final material properties, a relative difference of 171% can be observed for the $12 \times 12 \text{ mm}^2$ geometry.

Table 9 Summarized statistical evaluation of the joint modulus E_{joint}

Geometry	Adhesive condition	Number of specimens	E_{joint}			
			Min [MPa]	$\bar{x}_{E_{\text{joint}}}$ [MPa]	Max [MPa]	Std dev [MPa]
12 × 12	Initial	12	4.12	4.83	5.53	0.45
12 × 12	Inter	18	3.68	7.63	10.46	2.30
12 × 12	Final	18	7.85	13.06	16.87	2.36
8 × 24	Initial	6	7.34	8.20	8.71	0.47
8 × 24	Inter	12	9.61	15.26	16.67	1.85
8 × 24	Final	12	16.84	19.40	21.35	1.41

For the specimens with $8 \times 24 \text{ mm}^2$ joint dimensions, an increase in stiffness of 137% could be determined.

The differences between the adhesive conditions are significantly more pronounced in the stiffness compared to the ultimate fracture stress σ_{ult} . In contrast to the influence on the strength parameters, where the second production batch results in a lower ultimate fracture stress σ_{ult} , the joint modulus E_{joint} is increased in this series.

4 Conclusion and future research

This publication investigated the influence of the manufacturing and curing process on SG adhesives. For the economical manufacturing of the modified H-specimens, T-profiles made from raw aluminum were used as the substrate due to easy machining and low cost. Within the framework of the investigations, a 100% cohesive failure pattern could be determined for all specimens. Thus, the manufacturing of the specimens with this material does not seem to influence the results of the load-bearing capacity tests. By using the T-profiles, a rigid connection to the testing machine could be achieved, making it possible to determine the stiffness behavior of the joints accurately. The demonstrated manufacturing method shows very low variation in results for specimens within the same series.

Within the scope of the central investigations, it was possible to determine that the adhesive's curing state significantly influences the strength and stiffness properties. The specimen age and the selected curing method had a relevant influence on the adhesive condition and, thus, the load-bearing properties. It was possible to define the specimens' minimum age to

obtain final adhesive properties, depending on the curing method. Here it could be shown that the storage of 28 days described in (ETAG 002-1) seems sufficient but can be shortened to 21 days by tempering the adhesive. The failure pattern for both joint geometries confirmed the difference in the adhesive condition.

Following the fundamental analysis of the influence of manufacturing and curing, material parameters for the calculation methods used in practice, like the structural spring method, were determined. For a detailed description of the influences due to manufacturing and curing, a good analysis of the influences was possible by using boxplot diagrams.

All specimens were grouped into three adhesive conditions to define the statistically validated material parameters. Considering the two investigated joint geometries, no relevant influence on the strength of the joints could be determined. For all specimens, after 7 days, the strength of 0.7 MPa required by (ETA-01/0005) to transport the manufactured elements could be achieved. With the final properties, a 20% higher characteristic breaking stress σ_k compared to the manufacturer's specifications of $\sigma_k = 6 \times 0.14 = 0.84 \text{ MPa}$ could be determined. It should be mentioned here that this only applies to adhesives processed under controlled conditions from industrial mixing plants and cannot be transferred to other adhesive systems.

After validation by further research, this may be an impetus to increase the characteristic breaking stress σ_k and the associated design stress σ_{des} in the future. With this increase in the characteristic breaking stress σ_k , a more economical design of SG joints is possible without adjusting the level of the safety or method factor γ , which is already frequently discussed. Within the scope of further investigations, the behavior under high

and low temperatures and after artificial aging should be analyzed in particular. For the investigations of the residual strength after artificial aging, (ETAG 002-1) specifies a minimum strength of 75% compared to the strength tested at RT. The load-bearing behavior under shear load is also not part of these investigations.

An overview of the available calculation methods was given to determine stiffness properties. The extended FKG method was used to determine the joint modulus E_{joint} to analyze the influence of manufacturing and curing. This calculation method provides material parameters that well describe the deformation range modeled within the scope of calculations by the structural spring model. A significant influence on the stiffness could be determined by both the curing condition and the joint geometry.

The influence of the variation of the stiffness properties on the results in a static calculation was not investigated within the scope of this publication. This influence should be determined in future research. In addition, alternative, especially nonlinear, methods for more accurate stiffness determination could be considered, as well as the influence due to the variation of the evaluation limits. However, the accuracy of such calculations can be significantly increased in the future with the help of the realistic joint properties in dependence on the joint geometry and adhesive condition defined in this publication.

Acknowledgements The authors would like to thank *seele GmbH* gratefully for their support during the studies by providing us with adhesive and the possibility to manufacture the specimens.

Funding Open Access funding enabled and organized by Projekt DEAL. No funding was received for conducting this study.

Declarations

Conflict of interest On behalf of all authors, the corresponding author states that there is no conflict of interest.

Open Access This article is licensed under a Creative Commons Attribution 4.0 International License, which permits use, sharing, adaptation, distribution and reproduction in any medium or format, as long as you give appropriate credit to the original author(s) and the source, provide a link to the Creative Commons licence, and indicate if changes were made. The images or other third party material in this article are included in the article's Creative Commons licence, unless indicated otherwise in a credit line to the material. If material is not included in the article's Creative Commons licence and your intended use is not

permitted by statutory regulation or exceeds the permitted use, you will need to obtain permission directly from the copyright holder. To view a copy of this licence, visit <http://creativecommons.org/licenses/by/4.0/>.

References

- ASTM C1401-14. Standard guide for structural sealant glazing. ASTM International (2014)
- Beech, D.G., Owen, D.B.: Handbook of Statistical Tables Applied Statistics vol. 11(3), p. 211 (1962). <https://doi.org/10.2307/2985368>
- Bues, M., Schuler, C., Albiez, M., Ummerhofer, T., Fricke, H., Vallée, T.: Load bearing and failure behaviour of adhesively bonded glass-metal joints in façade structures. *J. Adhes.* **95**(5–7), 653–674 (2019). <https://doi.org/10.1080/00218464.2019.1570158>
- Bues, M.D.: Ein Beitrag zur Auslegung tragender Klebverbindungen im Fassadenbau. Dissertation, Karlsruher Institut für Technologie (KIT) (2021)
- Descamps, P., Hayez, V., Chabih, M.: Next generation calculation method for structural silicone joint dimensioning *Glass. Struct. Eng.* **2**(2), 169–182 (2017). <https://doi.org/10.1007/s40940-017-0044-7>
- Descamps, P., van Wassenhove, G., Hayez, V.: Simulating structural silicone glazing joint deformation with spring models *glass. Struct. Eng.* **5**(2), 171–185 (2020). <https://doi.org/10.1007/s40940-019-00105-6>
- Descamps, P., Hayez, V.: Silicone joint dimensioning calculation methods, In: Challenging Glass Conference Proceedings: Challenging Glass, vol. 6, pp. 337–350 (2018). <https://doi.org/10.7480/CGC.6.2156>
- Dias, V., Odenbreit, C., Hechler, O., Scholzen, F., Ben Zineb, T.: Development of a constitutive hyperelastic material law for numerical simulations of adhesive steel–glass connections using structural silicone. *Int. J. Adhes. Adhes.* **48**, 194–209 (2014). <https://doi.org/10.1016/j.ijadhadh.2013.09.043>
- DIN EN 13022-1:2014-08. Glas im Bauwesen—Geklebte Verglasungen—Teil 1: Glasprodukte für Structural-Sealant-Glazing (SSG-) Glaskonstruktionen für Einfachverglasungen und Mehrfachverglasungen mit oder ohne Abtragung des Eigengewichtes. Beuth Verlag GmbH, Berlin (2014)
- DIN EN 1990:2010-12. Eurocode: Grundlagen der Tragwerksplanung. Beuth Verlag GmbH, Berlin (2010)
- DIN EN ISO 527. Kunststoffe—Bestimmung der Zugeigenschaften. Beuth Verlag GmbH, Berlin (2019)
- Drass, M.: Constitutive Modelling and Failure Prediction for Silicone Adhesives in Façade Design, vol. 55. Springer, Wiesbaden (2020)
- Drass, M., Kraus, M.A.: Dimensioning of silicone adhesive joints: eurocode-compliant, mesh-independent approach using the FEM. *Glass Struct. Eng.* **5**(3), 349–369 (2020a). <https://doi.org/10.1007/s40940-020-00128-4>
- Drass, M., Kraus, M.A.: Semi-probabilistic calibration of a partial material safety factor for structural silicone adhesives—part I: derivation. *Int. J. Struct. Glass Adv. Mater. Res.* **4**(1), 56–68 (2020b). <https://doi.org/10.3844/sgamrsp.2020.56.68>

- EN 13830:2015+A1:2020. Curtain walling—product standard (2020)
- ETA-01/0005. Sealant used in structural sealant glazing systems to bond glass onto metal. EOTA, Brussels (2017)
- ETAG 002 - 1. GUIDELINE FOR EUROPEAN TECHNICAL APPROVAL FOR STRUCTURAL SEALANT GLAZING KITS (SSGK). EOTA, Brussels (2012)
- Fachverband Konstruktiver Glasbau e.V. Technical Note FKG 01/2021—Structural Silicone Sealants in Structural Glass Systems (21.09.21)
- Feynman, R.P., Leighton, R.B., Sands, M.L. Mainly electromagnetism and matter. In: The Feynman Lectures on Physics, vol. 2. Feynman, Leighton, Sands, Basic Books, New York (2010)
- Gent, A.N.: Engineering with Rubber: How to Design Rubber Components, 3rd edn. Carl Hanser Fachbuchverlag (2012)
- Habenicht, G. Kleben: Grundlagen, Technologien, Anwendungen. Springer, Berlin, Heidelberg (2009)
- Hagl, A.: Die Innovation—Kleben: Aktuelles aus der “Arbeitsgruppe Kleben” des Fachverbandes Konstruktiver Glasbau—FKG. Stahlbau **75**(6), 508–520 (2006). <https://doi.org/10.1002/stab.200610054>
- Hagl, A.: Bemessung Von Strukturellen Silikon-Klebung. Stahlbau **76**(8), 569–581 (2007). <https://doi.org/10.1002/stab.200710060>
- ISO 16269-6:2014-01. Statistical interpretation of data—part 6: determination of statistical tolerance intervals. Beuth Verlag GmbH (2014)
- ISO 527-1:2019. Plastics—Determination of tensile properties. Beuth Verlag GmbH, Berlin (2019)
- Kraus, M., Drass, M.: Semi-probabilistic calibration of a partial material safety factor for structural silicone adhesives—part II: verification concept. Int. J. Struct. Glass Adv. Mater. Res. **4**(1), 10–23 (2020). <https://doi.org/10.3844/sgamrsp.2020.10.23>
- Loch, M.: Beitrag zur Bestimmung von charakteristischen Werkstofffestigkeiten in Bestandtragwerken aus Stahlbeton, Technische Universität Kaiserslautern (2014)
- Maniatis, I., Siebert, G., Nehring, G.: Dimensionierung von Klebefugen aus Silikon mit beliebiger Geometrie. Stahlbau **84**(S1), 293–302 (2015). <https://doi.org/10.1002/stab.201590086>
- Martins, P.A.L.S., Natal Jorge, R.M., Ferreira, A.J.M.: A Comparative study of several material models for prediction of hyperelastic properties: application to silicone-rubber and soft tissues. Strain **42**(3), 135–147 (2006)
- Meunier, L., Chagnon, G., Favier, D., Orgéas, L., Vacher, P.: Mechanical experimental characterisation and numerical modelling of an unfilled silicone rubber. Polym. Test. **27**(6), 765–777 (2008). <https://doi.org/10.1016/j.polymertesting.2008.05.011>
- Müller, P., Siebert, G., Schuler, C.: Einfluss der Fertigung auf das Tragverhalten von SG-Klebung. In: Glas im konstruktiven Ingenieurbau 18 (GIKI18). Glas im konstruktiven Ingenieurbau, München, 02.03.2023–03.03.2023 (2023)
- Richter, C., Abeln, B., Schaaf, B., Feldmann, M.: Vereinfachte Rechnerische Last-Verformungsvorhersage Von Klebfugen Mit Hyperelastischem Verhalten Im Konstruktiven Glasbau. Ce/pap **4**(1), 94–104 (2021). <https://doi.org/10.1002/cepa.1245>
- Richter, C.H.O.: Vereinfachte rechnerische Last-Verformungsvorhersage von Klebfugen mit hyperelastischem Verhalten im konstruktiven Glasbau. Dissertation, 1st edn. Schriftenreihe des Lehrstuhls für Stahlbau und Leichtmetallbau der RWTH Aachen, Heft 84. Shaker Verlag, Aachen (2018)
- Rosendahl, P.L.: From bulk to structural failure: fracture of hyperelastic materials, UNSPECIFIED (2020)
- Santarsiero, M. Laminated Connections for Structural Glass Applications. Dissertation, École Polytechnique Fédérale de Lausanne (2015)
- Schuler, C., Albiez, M., Bues, M., Ehard, H., Ummerhofer, T.: Tragende Klebverbindungen im Stahl-, Glas- und Fasadensbau. In: Kuhlmann, U. (ed.) Stahlbau Kalender, pp. 587–642. Wiley (2019)
- Schuler, C., Mayer, B., Ummerhofer, T., Albiez, M., Bues, M., Vallée, T., Fecht, S. Systematische Untersuchung des Trag- und Versagensverhaltens geklebter Stahl-Glas-Verbindungen (SG): IGF-Vorhaben 18211 N/FOSTA P 1052, Schlussbericht (2017)
- Staudt, Y., Odenbreit, C., Schneider, J.: Failure behaviour of silicone adhesive in bonded connections with simple geometry. Int. J. Adhes. Adhes. **82**, 126–138 (2018). <https://doi.org/10.1016/j.ijadhadh.2017.12.015>
- The Mathworks, Inc. MATLAB - Box chart (box plot) - Help Center. <https://de.mathworks.com/help/matlab/ref/boxchart.html> (2022). Accessed 5 May 2022
- Treloar, L.R.G. The physics of rubber elasticity: by Treloar, L.R.G., 3rd edn. Oxford Classic Texts in the Physical Sciences Series. Oxford University Press, Oxford (1975)
- van Lancker, B., Dispersyn, J., de Corte, W., Belis, J.: Durability of adhesive glass-metal connections for structural applications. Eng. Struct. **126**, 237–251 (2016). <https://doi.org/10.1016/j.engstruct.2016.07.024>
- van Lancker, B., de Corte, W., Belis, J.: Calibration of hyperelastic material models for structural silicone and hybrid polymer adhesives for the application of bonded glass. Constr. Build. Mater. **254**, 119204 (2020). <https://doi.org/10.1016/j.conbuildmat.2020.119204>
- Wallau, W., Recknagel, C., Smales, G.J.: Structural silicone sealants after exposure to laboratory test for durability assessment. J. Appl. Polym. Sci. **138**(35), 50881 (2021). <https://doi.org/10.1002/app.50881>
- White, C.C., Hunston, D.L., Tan, K.T., Filliben, J.J., Pintar, A.L., Schueneman, G.: A systematic approach to the study of accelerated weathering of building joint sealants. J. ASTM Int. **9**(5), 1–17 (2012)

Publisher's Note Springer Nature remains neutral with regard to jurisdictional claims in published maps and institutional affiliations.